

Measuring the mass accretion rates of Herbig Ae/Be stars with X-shooter *

M. A. Pogodin^{1,2,**}, S. Hubrig³, R. V. Yudin^{1,2}, M. Schöller⁴, J. F. González⁵, and B. Stelzer⁶

¹ Central Astronomical Observatory at Pulkovo, St. Petersburg 196140, Russia

² Isaac Newton Institute of Chile, Saint-Petersburg Branch, Russia

³ Leibniz-Institut für Astrophysik Potsdam, An der Sternwarte 16, 14482 Potsdam, Germany

⁴ European Southern Observatory, Karl-Schwarzschild-Str. 2, 85748 Garching, Germany

⁵ Instituto de Ciencias Astronomicas, de la Tierra, y del Espacio (ICATE), 5400, San Juan, Argentina

⁶ INAF-Osservatorio Astronomico di Palermo, Piazza del Parlamento 1, 90134 Palermo, Italy

Received date / Accepted date

Key words techniques: spectroscopic – stars: accretion, accretion disks – stars: pre-main sequence – (stars:) circumstellar matter – stars: magnetic fields – stars: individual (HD 97048, HD 100546, HD 101412, HD 135344B, HD 150193, HD 176386, HD 190073, PDS 2)

We present the results of our observations of eight magnetic Herbig Ae/Be stars obtained with the X-shooter spectrograph mounted on UT2 at the VLT. X-shooter provides a simultaneous, medium-resolution and high-sensitivity spectrum over the entire wavelength range from 300 to 2500 nm. We estimate the mass accretion rates (\dot{M}_{acc}) of the targets from 13 different spectral diagnostics using empiric calibrations derived previously for T Tauri-type stars and brown dwarfs. We have estimated the mass accretion rates of our targets, which range from 2×10^{-9} to $2 \times 10^{-7} M_{\odot}/\text{yr}$. Furthermore, we have found accretion rate variability with amplitudes of 0.10–0.40 dex taking place on time scales from one day to tens of days. Additional future night-to-night observations need to be carried out to investigate the character of \dot{M}_{acc} variability in details. Our study shows that the majority of the calibrational relations can be applied to Herbig Ae/Be stars, but several of them need to be re-calibrated on the basis of new spectral data for a larger number of Herbig Ae/Be stars.

© 2010 WILEY-VCH Verlag GmbH & Co. KGaA, Weinheim

1 Introduction

Herbig Ae/Be stars (HAeBes) are pre-main sequence (PMS) objects of intermediate mass approximately from 2 to $10 M_{\odot}$ (Herbig 1960; Finkenzeller & Mundt 1984). They range from spectral class F2–O9 and are surrounded by relict dust/gas accretion disks, reflecting themselves in the form of an IR excess as a result of thermal emission of circumstellar (CS) dust. For a number of stars, the disks can also be directly detected on images (e.g. Grady et al. 2005). The CS environment of HAeBes possesses a complex structure. Gaseous streams are accreted from the equatorial disk onto the star and a stellar wind zone exists at higher latitudes. On the other hand, the disk wind, the so-called magnetocentrifugal wind, carries the excess of angular momentum away (e.g. Garcia et al. 2001). CS contribution to the stellar atmospheric spectrum provides information on physical processes in the envelope and on its interaction with the star. The character of this interaction is reasonably well studied for PMS objects with masses of about one solar mass and less (T Tauri-type stars or TTS). These objects have significant (several kG) dipole-type magnetic fields. The star/CS interaction in TTS is described in de-

tail by the model of magnetospheric accretion (MA; e.g. Bouvier et al. 2007, and references therein). According to the MA-model, the field truncates the disk where the ram pressure of the accreted matter is balanced by pressure from the stellar magnetic field. At the truncation radius the accreted material is channeled into funnel flows and ballistically falls onto the stellar surface. A situation that is less clear for HAeBes. Their interiors are mostly radiative (see e.g. Fig. 8 in Hubrig et al. 2009). However, convection is needed to maintain a stellar dynamo that generates a strong magnetic field. Nevertheless, most late-type HAeBes with spectral classes later than B9 (HAes), have possibly evolved from the so-called intermediate mass T Tauri stars (IMTTS) of K–G spectral types (see e.g. Palla & Stahler 1993) possessing sub-atmospheric convective zones and, as a result, strong magnetic fields. It is likely that these fields do not dissipate completely during the PMS evolutionary stage. Additionally, it is possible that magnetic fields of HAeBes are generated by differential rotation of the star or originate in dynamos within the CS disk (Tout & Pringle 1995; Tout & Pringle 1996). Recent direct measurements of HAeBe magnetic fields using spectropolarimetry (Wade et al. 2007; Hubrig et al. 2007, 2009, 2011a, and references therein) have allowed to detect longitudinal magnetic fields of hundreds of Gauss in a number of HAes. Stars for which so far no magnetic field could be detected may still have a field

* Based on observations obtained at the European Southern Observatory, Paranal, Chile (ESO programme 385.C-0131(A)).

** Corresponding author: e-mail: pogodin@gao.spb.ru

but below the current sensitivity limits. The inner boundary of their accretion disks are likely to be located close to the stellar surface.

The existence of magnetically controlled disk accretion in HAes going through polar funnels was confirmed by Muzerolle et al. (2004), Mottram et al. (2007), and Grady et al. (2010). In any case, the magnetospheric radii of HAes with $B \approx 100$ G must be much smaller in comparison with those of TTS, where magnetic fields are of the order of several kG. As a result, we can expect the character of the star/CS interaction in HAes to be different from that of TTS. In our study aim at investigating the general picture of the star/CS interaction in HAes and at comparing it with that in TTS. One of the initial goals was also to study the variations of the accretion mass rates over the magnetic period. However, due to weather or technical constraints the observations were carried out mostly for targets with single magnetic field measurements, i.e. for targets with unknown magnetic phase curves. Clearly, an analysis of the temporal behaviour of different mass accretion rate indicators over the magnetic/rotation periods would provide fundamental clues on how magnetospheric accretion works. The targets for which magnetic/rotation periods have been determined in our previous studies include HD 97048 and HD 101412 with only one X-shooter observations, respectively, HD 150193 with two observations, and HD 176386 with four observations (Hubrig et al. 2011b, 2011a).

One of the most important parameters characterizing the properties of the star/CS interaction is the mass accretion rate \dot{M}_{acc} . It determines strongly the disk structure and dynamics (e.g., D'Alessio et al. 1999, 2001). Measurements of \dot{M}_{acc} are well-developed for TTS, based on a number of empirical spectral diagnostics (e.g., Oudmaijer et al. 2011, Rigliaco et al. 2011, and references therein).

Three main purposes of our work presented here are:

1. To determine \dot{M}_{acc} in a sample of HAes whose magnetic fields have been detected (Hubrig et al. 2009, 2011b) using calibrations previously obtained for TTS and brown dwarfs (BDs). Magnetic HAes appear to be most suitable targets for such a study because their disk accretion process is expected to better fit the MA scenario in comparison with non-magnetic stars.
2. To test the applicability of different calibrations for measuring \dot{M}_{acc} of HAes and to select the best spectroscopic tracers of accretion necessary to provide accurate accretion rates for systematic studies of large samples of HAes.
3. To search for variability of \dot{M}_{acc} in HAes with more than one available spectrum. This variability can be twofold: a) a real change in the accretion process, and b) a modulation of \dot{M}_{acc} by the rotating magnetosphere and a cyclic screening of the stellar limb by local funnel streams.

2 Mass accretion rate calibrations

2.1 Calibrations for TTS and BDs

At present, a number of empiric spectral indicators are available for the determination of \dot{M}_{acc} for TTS and BDs.

2.1.1 Model method

The basic accretion indicator is the additional emission in the continuum superimposed onto the stellar spectrum and calculated on the basis of MA models for these objects (e.g., Calvet & Gullbring 1998, Gullbring et al. 2000, Ardila et al. 2002). It is assumed that the overwhelming bulk of this emission originates in funnel flows inside the magnetosphere and in the shock zone on the stellar surface in a compact region. This assumption is rather plausible since the emissivity in the continuum is proportional to N_e^2 (where N_e is the electron density), and the magnetospheric streams consist of the densest CS matter. The gas density in other parts of the envelope (disk and wind) drops very quickly with distance from the star, and its contribution to the additional continuum emission is negligible. In the observed spectra, this emission is seen as veiling of the atmospheric lines and as an excess radiation at wavelengths below the Balmer jump. The theoretical models allow to construct a quantitative relation between \dot{M}_{acc} and the veiling plus UV excess. Yet, veiling and UV excess frequently prove not to be convenient for these measurements, due to the large extinction in the regions where the targets are located.

2.1.2 L - type calibrations

Alternatively, empirical calibrations have been determined between emission lines and mass accretion.

All emission lines in the spectrum of a PMS object are of multi-component origin. They are formed not only in the magnetospheric streams, but also in the disk and in the wind. The source function determining the emissivity in a line drops with the distance from the star much slower than the emissivity in the continuum (for example, see Pogodin 1986, 1989 for Balmer emission lines). However, according to the MA models, such parameters as the mass of the star, mass of the disk, \dot{M}_{acc} and mass loss rate \dot{M}_{wind} are likely to be interdependent. It has been established that the accretion luminosity (L_{acc}) is clearly correlated with luminosity in some emission lines (L_{line}). A number of empirical calibrations have been published so far. The dependencies are approximated by expressions of the type:

$$\log(L_{\text{acc}}) = a \log(L_{\text{line}}) + b, \quad (1)$$

$$\dot{M}_{\text{acc}} = \frac{L_{\text{acc}} R_*}{GM_*}, \quad (2)$$

where M_* and R_* are the stellar mass and radius, respectively, and a and b are coefficients determined separately for each spectral line (e.g., Fang et al. 2009, Dahm 2008, Herczeg & Hillenbrand 2008, Gatti et al. 2008, Natta

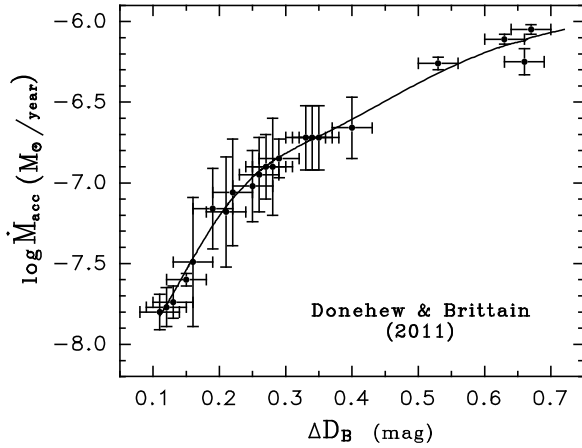


Fig. 1 Relationship between ΔD_B and \dot{M}_{acc} constructed on the base of data extracted from Table 3 in Donehew & Brittain (2011) and fitted by a polynomial.

et al. 2004, Mohanty et al. 2005). The calibrations are constructed on the basis of spectroscopic observations of the chosen line in a representative sample of targets, whose \dot{M}_{acc} values were determined beforehand using the model method.

2.1.3 F - type calibrations

Besides of that, another type of empirical calibrations exists that is based on a direct correlation between \dot{M}_{acc} and the flux in the emission line (F_{line}). The dependencies are expressed as:

$$\log(\dot{M}_{\text{acc}}) = c \log(F_{\text{line}}) + d, \quad (3)$$

where c and d are coefficients (e.g. Herczeg & Hillenbrand 2008). The F-type calibrations are constructed analogous to the case of L-type calibrations where the values of \dot{M}_{acc} are derived beforehand using the model method or from other types of calibration.

2.1.4 H α 10% - indicator

There is also a separate accretion indicator, the H α 10%. It is defined as the full width W of the emission H α profile at the level of 10% of the maximum intensity (White & Basri 2003). Natta et al. (2004) extended this indicator to very low-mass objects, where \dot{M}_{acc} was determined by fitting the observed H α profiles with predictions of MA models (Muzerolle et al. 2001). The calibration is expressed in the form:

$$\log(\dot{M}_{\text{acc}}) = c_1 \log(W(\text{H}\alpha 10\%)) + d_1, \quad (4)$$

where c_1 and d_1 are coefficients and $W(\text{H}\alpha 10\%)$ is given in (km/s) (Natta et al. 2004)

2.2 Calibrations for H AeBes

At present, calibrations constructed specifically for H AeBes are small in number.

Donehew & Brittain (2011) derived \dot{M}_{acc} for a considerable sample of H AeBes using the model method, where the modeling was applied to the emission Balmer jump ΔD_B . They calculated \dot{M}_{acc} in dependence of the emission Balmer jump for more than 30 H AeBes using the models and methods developed by Calvet & Gullbring (1998), Gullbring et al. (2000), and Muzerolle et al. (2004). The model of Muzerolle et al. (2004) takes into account the main physical processes predicted by the MA model such as: a ballistical infall of material from the disk onto the stellar surface along accretion columns, heating of the photosphere due to its shock interaction with the accretion streams and releasing soft X-rays that are absorbed by the surrounding material. This material then emits optical and UV radiation as it thermalizes. In the model, the flux from accretion is calculated for three different regions: the shock region, the heated photosphere, and the accretion columns, to get the overall flux from accretion, which is a function of M_* , R_* , and \dot{M}_{acc} . The resulting spectral energy distribution (SED) including both the accretion and the stellar flux is used to calculate the expected emission Balmer jump ΔD_B for different \dot{M}_{acc} and stars of different spectral types. The value of ΔD_B was defined as the difference in D_B (Balmer jump) for a given star from that of a standard (non-accreting) star of the same spectral type, where ΔD_B is the difference in the magnitudes at both sides of the discontinuity. The relationship between ΔD_B and L_{acc} calculated by Muzerolle et al. (2004) and between L_{acc} and \dot{M}_{acc} given in Sect. 2.1.2 were used by Donehew & Brittain (2011) to determine \dot{M}_{acc} of their program stars with different M_* and R_* . They used the expression:

$$\Delta D_B = 2.5 \log \frac{F_* + F_A}{F_*}. \quad (5)$$

The observational ΔD_B for all targets have been measured in the observed spectra normalized to the flux F_λ at 4000 Å using the spectra of standard stars and the Castelli-Kurucz LTE models (Castelli & Kurucz 2008) of stellar atmospheres with corresponding T_{eff} and $\log g$. As it turned out, the observational ΔD_B demonstrated a very convincing correlation with theoretical \dot{M}_{acc} . This result is likely to be related to the fact that the M_*/R_* -ratio is practically the same in PMS stars from late-B to K types with a dispersion of ± 0.1 dex. We have built the dependence between ΔD_B and \dot{M}_{acc} using the data taken from Columns 2 and 3 of Table 3 in Donehew & Brittain (2011) and fitting them by a polynomial. This relation is shown in Fig. 1 of this paper and used in our study.

Donehew & Brittain (2011) measured also the equivalent widths of the Br γ emission line and constructed the empiric correlation between $\log(L_{\text{acc}})$ (determined from ΔD_B) and $L_{\text{Br}\gamma}$. They concluded that this relationship is different for H Aes and for earlier type H AeBes (HBes)

and that the correlation for HAes is in satisfactory agreement with the calibration constructed earlier by Calvet et al. (2004) for classical TTS (CTTS) and IMTTS. Therefore, it appears that the Br γ emission line is probably a reliable tracer of \dot{M}_{acc} in HAes. One of the goals of our study is testing the reliability of additional available spectral indicators.

Also Garcia Lopez et al. (2006) determined \dot{M}_{acc} for 36 HAes using a similar calibration for TTS. Eight objects are in common between their target list and the list of Donehew & Brittain (2011). For four objects the agreement in the derived \dot{M}_{acc} values is rather good with $\Delta \log \dot{M}_{\text{acc}}$ ranging from 0.01 to 0.23 dex. Four other objects demonstrate significant differences from 0.7 to 1.2 dex. As a whole, the difference between the results of these two works makes up -0.18 ± 0.75 dex, where the error is the standard deviation. Taking into account that the accuracy of an individual estimate is of the order of ± 0.4 – 0.5 dex in both papers, the conclusion can be made that the results obtained in these two works demonstrate no significant difference.

During the time when our work was in preparation one additional paper was published by Mendigutia et al. (2011a), where a similar model method was used to determine mass accretion rates in 38 HAEs and the L-type calibrational relationships were constructed for several emission lines. We compared the results of this work with those obtained in Donehew & Brittain (2011) and Garcia Lopez et al. (2006). The Mendigutia et al. (2011a) sample has overlap with the target list of Donehew & Brittain (2011) – 14 stars – and with that of Garcia Lopez et al. (2006) – 13 stars. We see that \dot{M}_{acc} of about half the targets of Mendigutia et al. (2011a) are estimated to be systematically higher in comparison with those obtained in the two other studies ($+0.74 \pm 0.44$ dex for Donehew & Brittain 2011 and $+1.67 \pm 0.83$ dex for Garcia Lopez et al. 2006). Only upper limits of \dot{M}_{acc} have been obtained in Mendigutia et al. (2011a) for the second half of their targets. The differences in their \dot{M}_{acc} determinations with those obtained in the two other works account for more than -0.74 ± 0.56 dex compared to the work of Donehew & Brittain (2011) and -0.50 ± 0.24 dex compared to the work of Garcia Lopez et al. (2006).

Trying to understand the possible cause of these discrepancies, we compared the values of the emission Balmer jump ΔD_B measured in Mendigutia et al. (2011a) by a photometric method and in Donehew & Brittain (2011), where a spectroscopic method was used. We have obtained the difference 0.17 ± 0.17 . Taking into account the different dates of observations and different methods of measurements and their errors (± 0.07 for Mendigutia et al. 2011a and ± 0.03 for Donehew & Brittain 2011), we can conclude that the differences in these measurements are not essential.

Thus we assume that some systematic distinctions can be expected in a model calculating the relationship between \dot{M}_{acc} and ΔD_B carried out in the different studies. We note that \dot{M}_{acc} values determined in Mendigutia et al. (2011a) appear significantly overestimated: ten objects in their study

Table 1 Target stars for which X-shooter data were obtained during our observing run. Spectral type and photometric data were taken from the SIMBAD database.

Object	Spectral type	V	R	J	H	A_V
HD 97048	A0pshe	8.46	8.50	7.27	6.67	1.00
HD 100546	B9Vne	6.80	6.70	6.43	5.96	0.10
HD 101412	B9.5V	9.29	9.30	8.64	8.22	0.54
HD 135344B	F4–F8	7.85	7.83	7.31	6.67	0.10
HD 150193	A1Ve	8.88	8.90	6.95	6.21	1.60
HD 176386	B9IVe	7.30	–	6.90	6.75	0.60
HD 190073	A2IVpe	7.82	7.80	7.19	6.65	0.12
PDS 2	F2	10.73	–	10.01	9.68	0.55

present rates ranging from 10^{-4} to $10^{-6} M_{\odot}/\text{yr}$. Such large mass accretion rates can be expected only in protostars or in such unique objects as FUORs. In addition, according to the stellar masses and ages presented in Table 1 of Mendigutia et al. (2011a), six out of ten targets of the spectral type B8 – A2 are located on the HR diagram close to the main sequence where the accretion rates already become smaller than at earlier stages of the PMS evolution. Generally, the masses of accretion disks around HAEs range from 0.01 to $0.1 M_{\odot}$ (Hillenbrand et al. 1998, Henning et al. 1998, Natta et al. 2000). With mass accretion rates of the order of 10^{-4} to $10^{-6} M_{\odot}/\text{yr}$, the accretion disk would be completely dissipated already after 10^2 – 10^5 years. This time interval is much smaller than the time of the whole PMS evolution stage of objects with masses of $2 M_{\odot}$, which is about 10^6 years according to Palla & Stahler (1993).

Based on these results, the question arises whether calibrations determined for lower mass pre-main sequence stars, T Tauri stars, can be employed to estimate \dot{M}_{acc} in HAEs. Clearly, applicability of such calibrations for \dot{M}_{acc} in HAEs demands a special examination. It can be assumed that identical calibrations are applicable to HAEs provided that the character of the disk/magnetosphere and the disk/wind interaction in TTS and HAEs is similar and that the contribution of the CS regions to the whole CS spectrum formed in TTS and HAEs is comparable too. As was discussed in Sect. 1, the size of the magnetosphere and the value of B is expected to be much smaller in HAEs in comparison with TTS. It is not clear yet whether these differences have an impact on the relations between \dot{M}_{acc} and the emerging radiation in spectral lines.

3 Observations and data analysis

The observations were performed in service mode with the X-shooter spectrograph mounted on the 8 m UT2 of the VLT. X-shooter allows to obtain spectral data simultaneously over the entire wavelength range from the near-UV to the near-IR in three arms (the UVB-arm covering the range 300–590 nm, the VIS-arm 550–1000 nm, and the NIR-arm 1.0–2.5 μm). The observations were performed with the

Table 2 Stellar parameters of the targets. The majority of the data are taken from Hubrig et al. (2009). Further data is from; a – Catala et al. (2007); b – Montesinos et al. (2009); c – Coulson & Walter (1995); d – this work.

Object	T_{eff} [K]	$\log g$	M_*/M_\odot	R_*/R_\odot	$v \sin i$ km/s	$\langle B_z \rangle$ [G]
HD 97048	10000	4.0	2.5	2.2	140	188 ± 47
HD 100546	10500	4.5	2.5	1.5	65	89 ± 26
HD 101412	9500	4.0	2.5	2.7	5	-454 ± 42
HD 135344B	6250 ^c	4.0 ^c	1.36	1.9	70	-37 ± 12
HD 150193	9000	4.0	2.2	2.0	100	-252 ± 48
HD 176386	10000	4.0	2.7	2.3		-121 ± 35
HD 190073	9250	3.5	2.85 ^a	3.6 ^a 2.1 ^b	12	104 ± 19
PDS 2	7000 ^d	4.0 ^d	2.5	1.6	30 ^d	103 ± 29

Table 3 Non-accreting stars used as flux standards

Object	Spectral type	MJD	V
HD 100604	F2V	55352.008	7.69
HD 100627	F6IV/V	55408.332	8.49
HD 100926	A3III/IV	55466.170	9.75
HD 100928	A0IV	55648.147	9.52

highest possible spectral resolution, i.e. R is ~ 9100 in the UVB-arm, ~ 17400 in the VIS-arm, and ~ 11000 in the NIR-arm (D’Odorico et al. 2006). The data were reduced using the X-shooter pipeline (Version 1.1.0) following the standard steps. For more details see Modigliani et al. (2010). Due to a very high efficiency of the X-shooter spectrograph the signal-to-noise ratio (S/N) of 300–500 was achieved during exposure times ranging from 13–15 s for the brightest targets to 450 s for the faintest target PDS 2.

26 spectra of eight HAes with magnetic field detections were obtained during 13 nights distributed between May and September 2010. After each science exposure, telluric standards were automatically observed in Observatory time at $S/N \sim 100$. They are usually main-sequence hot stars or solar analogs. Further, the data package delivered by ESO includes a number of spectrophotometric standards. The flux standards used in our work are presented in Table 3.

The original observation request foresaw several observations per target over the rotation period, but due to technical problems with X-shooter and mediocre weather conditions, the program was only partially completed. The targets were chosen from the sample of Herbig Ae/Be stars investigated previously by (Hubrig et al. 2009). The list of X-shooter targets is presented in Table 1, and their stellar parameters together with the detected longitudinal magnetic fields are summarized in Table 2. Since the star PDS 2 was less intensively studied in the past than other targets, we estimated atmospheric parameters of this object by comparison between the observed spectrum in the range $\lambda\lambda 4460$ – 4500 \AA and the synthetic spectrum computed using the code SYNTH+ROTATE (Piskunov 1992). The best model fit is presented in Fig. 2 with parameters: $T_{\text{eff}} = 7000 \text{ K}$, $\log g =$

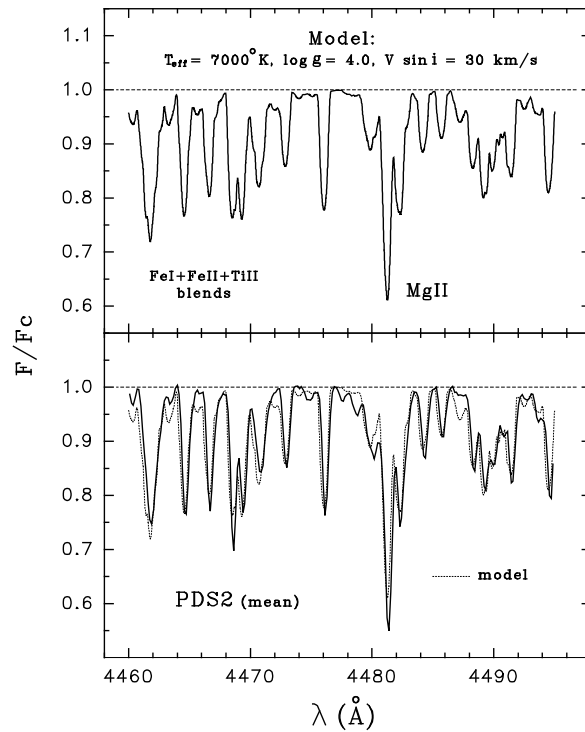


Fig. 2 Comparison of the mean observed spectrum of PDS 2 in the range of $\lambda\lambda 4460$ – 4500 \AA with the synthetic spectrum corresponding to the best fit. Top panel: The synthetic spectrum. Bottom panel: The overplotted observed spectrum (solid line) and the synthetic spectrum (dotted line).

4.0, and $v \sin i = 30 \text{ km/s}$. The complete list of observing dates is given in Table 5.

The data analysis concentrated on the emission lines and the emission Balmer jump that can be considered as accretion indicators. To remove telluric features, we used the telluric standards observed immediately after each observation at a similar zenith distance. The equivalent widths (EWs) of emission lines were measured after subtraction of stellar atmospheric profiles from the observed ones. The synthetic atmospheric profiles were calculated using the computer code

SYNTH+ROTATE (Piskunov 1992) and the standard LTE Kurucz models for the corresponding values of the stellar parameters (see Table 2). The synthetic atmospheric line profiles were also smoothed in accordance with the spectral resolution and $v \sin i$. For the near-IR hydrogen lines ($\text{Br}\gamma$, $\text{Pa}\beta$, and $\text{Pa}\gamma$), the excess of radiation was taken into account by comparing the photometric magnitudes of the target stars with those for unreddened stars of corresponding spectral type and a correction for A_λ using the standard extinction law. All necessary data for this step are presented in Table 1. The EWs of the Na I D lines were measured as a sum value for both components D_1 and D_2 , where the water vapour absorption lines and the interstellar (IS) narrow components were removed prior to this step. The IS components of the Na I D lines were cleaned by simple cutting. This procedure leads to a small underestimation of the EW, but it does not account for more than 10% (~ 0.1 dex) in the value of $\log \dot{M}_{\text{acc}}$. The emission lines of the IR Ca II triplet are blended by weak emission components of Pa13, Pa15, and Pa16. But their contribution to the EWs of the Ca II lines can be taken into account by polynomial interpolation of the EW(Pa-lines) using synthetic spectra based on the unblended Pa12, Pa14, and Pa17 lines (Fig. 6). We used standard LTE Castelli-Kurucz models (Castelli & Kurucz 2008) to determine fluxes at different wavelengths corresponding to lines chosen as accretion indicators for all program stars. The values of their stellar masses M_* and radii R_* were taken from Table 2 to calculate luminosities in the line-indicators.

The procedure of measuring the emission Balmer jump ΔD_B is illustrated in Fig. 3 using HD 100546 as an example. The ratio r of the initial unreddened spectra of the target (HD 100546) and the standard star of spectral type A0 (HD 100928) is approximated polynomially between 4000 Å and 4600 Å. The polynomial is extrapolated to 3640 Å and the ratio of ordinates r_2 and r_1 allows to determine the value of $\Delta D_B = 2.5 \log(r_2/r_1)$. This procedure is identical to that used in the work of Donehew & Brittain (2011).

4 Spectral accretion indicators

We examined 13 spectral diagnostics of \dot{M}_{acc} that have previously been used in studies of TTS and BD. The basic indicator was the emission Balmer jump ΔD_B , calculated by the method described in Sect. 3. We used the relation between ΔD_B and \dot{M}_{acc} presented in Fig. 1. Eight indicators, based on the measurements of L_{acc} include $\text{H}\alpha$, $\text{H}\beta$, $\text{He I } \lambda 5876$, $\text{Br}\gamma$, Na I D, $\text{Pa}\beta$, $\text{Pa}\gamma$, and Ca II $\lambda 8542$. We considered also three indicators where flux in an emission line was used for the direct determination of \dot{M}_{acc} according to eq. 3: He I $\lambda 5876$, Ca II $\lambda 8542$, and Ca II $\lambda 8662$. Further in the text we use the abbreviations “(L)” and “(F)” to mark indicators based on the measurements of L_{acc} and flux, respectively (e.g., $\text{Pa}\gamma$ (L), Ca II $\lambda 8662$ (F), etc.). The

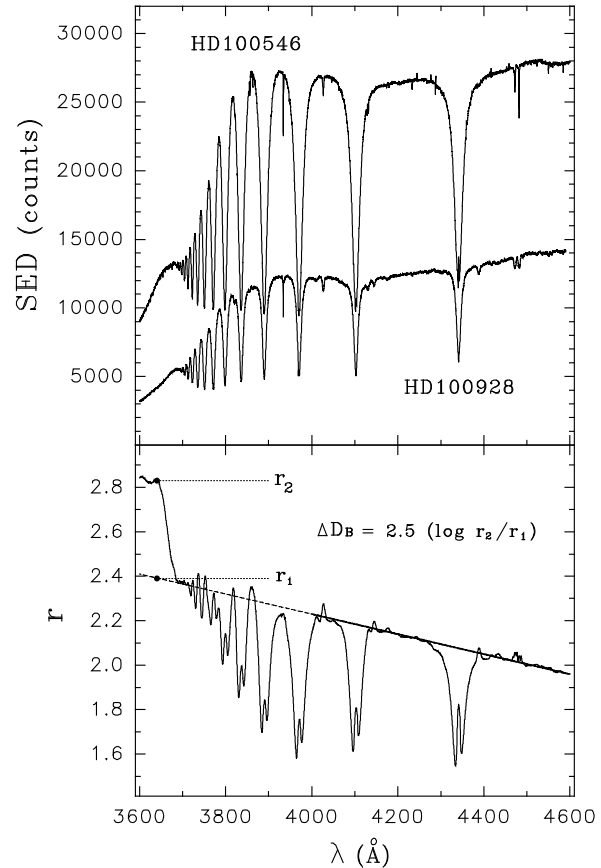


Fig. 3 Spectral energy distribution (SED) in the observed spectrum of HD 100546 and of the normal main-sequence star HD 100928 of spectral type A0V in the range of $\lambda\lambda 3600\text{--}4600\text{Å}$ covering the Balmer jump (top panel). The bottom panel illustrates the ratio $r = \text{SED}(\text{HD 100546})/\text{SED}(\text{HD 100928})$. The solid line marks the polynomial approximation of $r(\lambda)$ between $\lambda 4000\text{Å}$ and $\lambda 4600\text{Å}$, and the dotted line shows its extrapolation up to $\lambda 3640\text{Å}$. The formula for the calculation of the emission Balmer jump is also inserted.

last indicator is $\text{H}\alpha 10\%$, which was calibrated by Natta et al. (2004). All these diagnostics are presented in Table 4.

Selected regions of the observed spectra of the program stars are presented in Figs. 4 to 7.

4.1 $\text{H}\alpha$ emission

The emission $\text{H}\alpha$ profiles vary strongly from object to object (Fig. 4). HD 150193 and HD 190073 demonstrate PCyg-type profiles indicating the existence of a stellar wind between the star and the observer. The $\text{H}\alpha$ profiles of HD 100546 and HD 101412 are double-peaked with a central absorption shifted relative to the stellar rest wavelength of the line. The $\text{H}\alpha$ profile of HD 97048 is double-peaked too, but of a complex structure, and single emission profiles are observed in the spectra of HD 135433B and PDS 2.

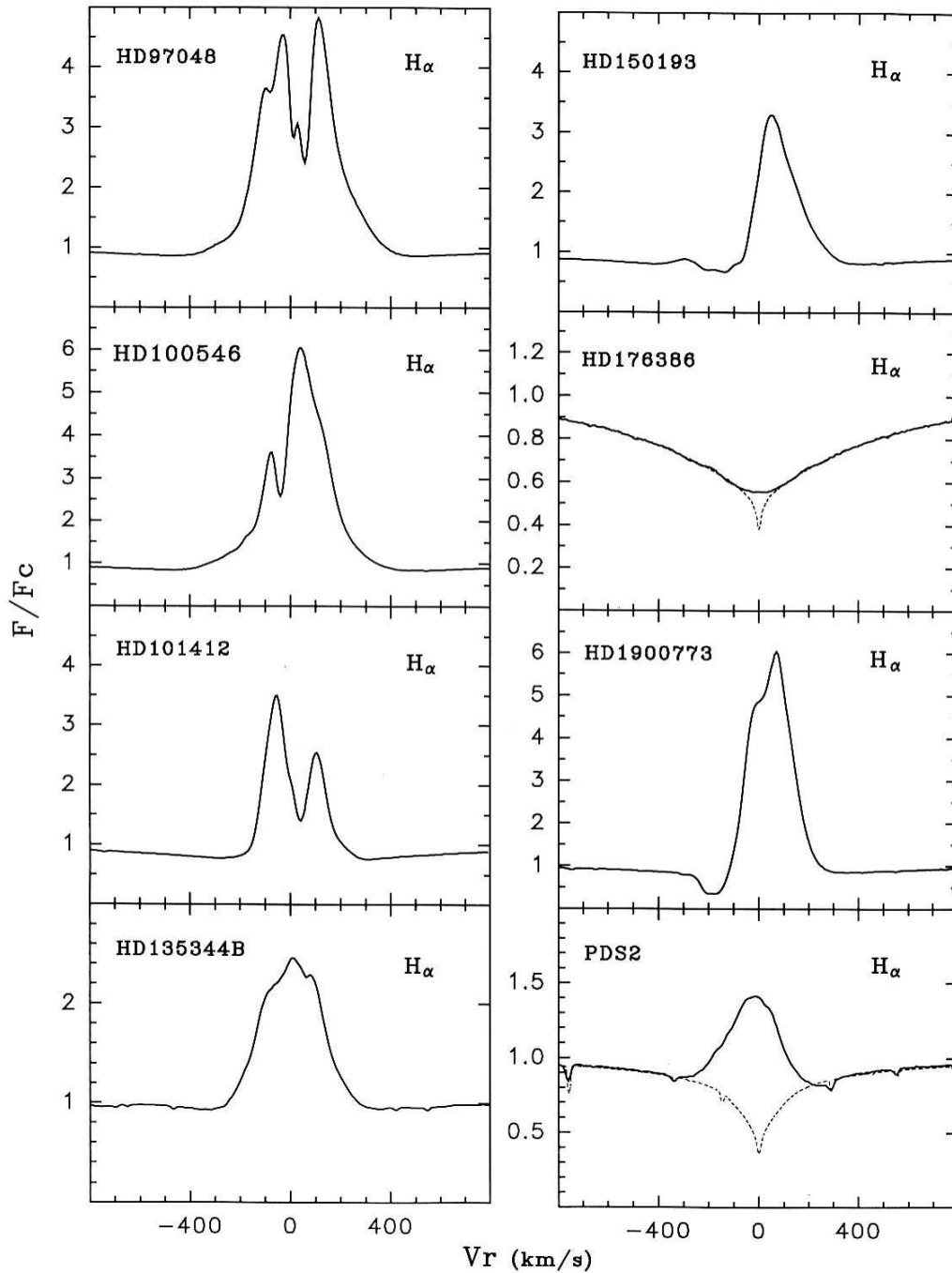


Fig. 4 Normalized $H\alpha$ profiles in the spectra of studied HAes. For HD 135344B, HD 150193, HD 176386, HD 190073, and PDS 2 the displayed profiles are observed on dates MJD55357.329, 371, 55352.047, 55465.138, 55446.078, and 55410.343, respectively. Profiles of HD 135344B and PDS 2 are shown in comparison with synthetic profiles calculated with the computer code SYNTH+ROTATE of (Piskunov 1992). The LTE models of Castelli & Kurucz (2008) are used for the stellar parameters listed in Table 2. In the case of PDS 2, the value $v \sin i = 30$ km/s was used to calculate the model profile.

Table 4 Mass accretion rate diagnostics that have been used in previous studies of TTs and BDs and are analyzed in this work

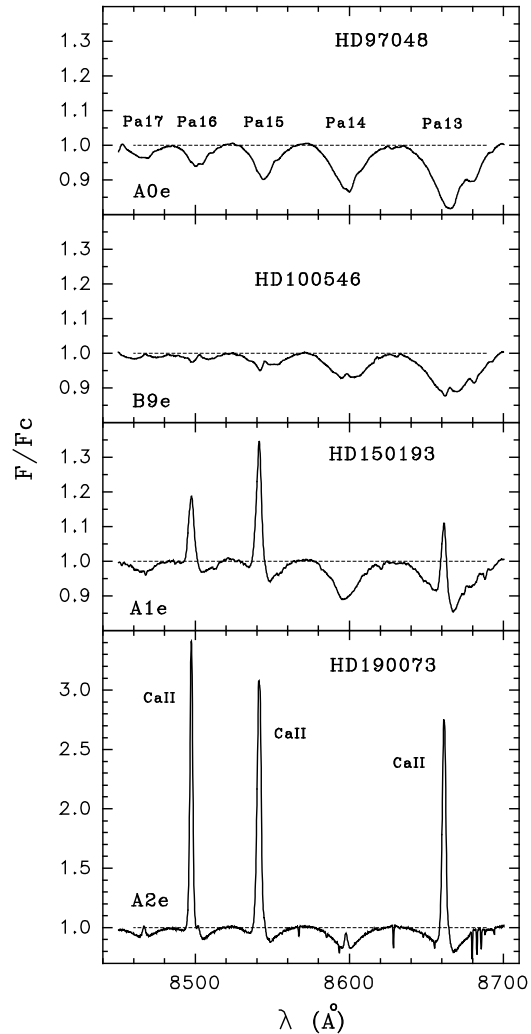
Reference	Diagnostic	Mass range [M_*/M_\odot]
Fang et al. (2009)	$H\alpha$ (L), $H\beta$ (L), He I $\lambda 5876$ (L)	0.1 – 2.0
Herczeg & Hillenbrand (2008)	Na I D (L), Ca II $\lambda 8542$ (F), Ca II $\lambda 8662$ (F), He I $\lambda 5876$ (F)	0.1 – 1.0
Dahm (2008)	$Pa\beta$ (L), $Pa\gamma$ (L), and Ca II $\lambda 8542$ (L)	0.5 – 2.0
Natta et al. (2004)	$Pa\beta$ (L), $H\alpha$ 10%	0.01 – 0.1
Gatti et al. (2008)	$Pa\beta$ (L), $Pa\gamma$ (L)	0.1 – 1.0

As can be seen in Fig. 4, the $H\alpha$ emission is practically invisible in the spectrum of the B9e star HD 176386. This fact was already discussed by other authors. Bibó et al. (1992) characterized this object as a higher-mass analog of so-called weak-line T Tauri stars (WTTS) with already dispersed accretion disks. On the other hand, Grady et al. (1993) report that signatures of a matter infall onto the star is observed in the UV spectrum of HD 176386. If the disk of HD 176386 is already dispersed, calibrations derived for the magnetospheric accretion scenario are no longer valid because the balance of the emission from different parts of the circumstellar components (magnetosphere, disk, wind) changes. In any case, the standard model of magnetospheric accretion from the disk can hardly be applied to this object. Therefore, any empirical spectral calibration based on the MA model cannot be used.

4.2 Other emission lines

Fig. 5 illustrates the spectra of the targets in the region of the He I $\lambda 5876$ and Na I D lines, and Fig. 6 in the region of the IR Ca II triplet. The emission profiles of He I $\lambda 5876$ are in general single-peak or double-peak type in the spectra of the HAeBes, but in some cases a deep redshifted absorption overlaps the red emission wing (see for more details Böhm & Catala 1995, Mendigutia et al. 2011b). An example of such a feature is seen in the spectrum of HD 97048 (Fig. 5). This line originates in the highest temperature regions of the CS envelope involving the inner boundary of the accretion disk interacting with the magnetosphere, the matter streams infalling onto the star, and the region of the impact of the streams on the stellar surface. These regions are rather compact in size and screening of the stellar limb by the accreted flows can be an important factor in forming the observed line profile. This screening leads to the appearance of a redshifted absorption component of the profile. Therefore, we have to be careful in using the He I emission for the \dot{M}_{acc} determination. At the time when the infalling stream screens the stellar limb, the \dot{M}_{acc} measurement can be considerably underestimated.

The types of the Na I D line profiles (Fig. 5) as well as of the IR Ca II triplet profiles (Fig. 6) in the spectra of the targets are very diverse. Even in objects of similar spectral types (A2–B9) are the intensities of these emission lines completely different. The emission in the Na I D lines is clearly visible and the EW can be measured in three objects

**Fig. 6** Normalized spectra of HD 97048, HD 100546, HD 150193, and HD 190073 in the spectral region containing near-IR Ca triplet lines. The positions of the Pa lines are indicated in the upper panel, and the positions of the Ca II lines in the lower panel. Strong emission near-IR Ca triplet lines appear only in two HAe stars, HD 150193 and HD 190073.

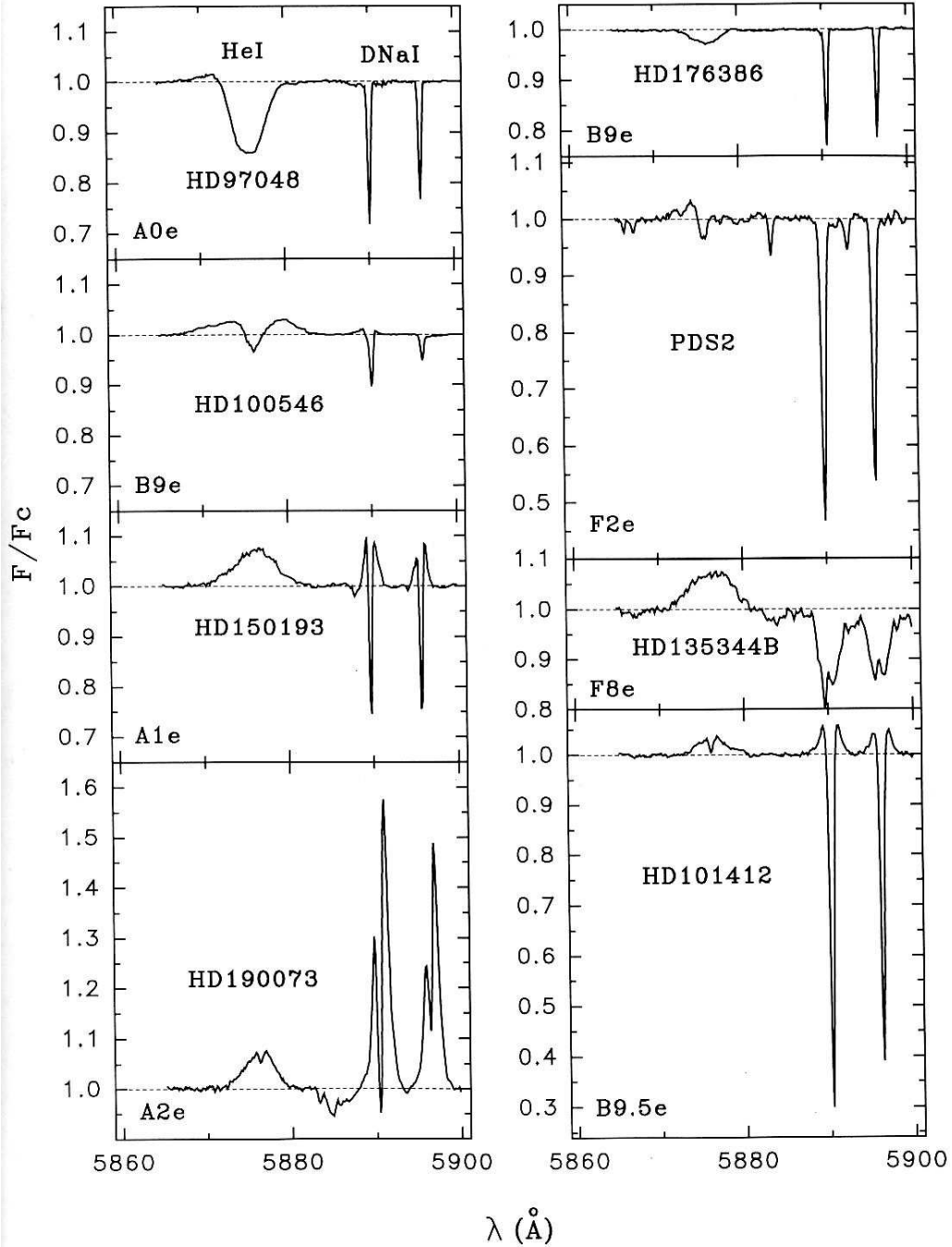


Fig. 5 The same as in Fig. 4, but for the spectral region around He I 5876 and Na I D.

(HD 190073, HD 150193, and HD 101412). As for the Ca II triplet, the EW can be measured only in HD 190073 and HD 150193. It is remarkable that in our sample HD 190073 is the star with the strongest intensities of the Na I D and IR Ca II lines. This object demonstrates the clearest developed PCyg-structure of the $H\alpha$ profile (Fig. 4). The second object with an $H\alpha$ profile of PCyg-type is HD 150193. It shows also rather intense emission in Na I D and IR Ca II. This fact leads us to the hypothesis that the appearance of considerable emission in the Na I D and IR Ca II lines is re-

lated to the presence of a wind zone between the star and the observer. The signatures of the matter outflow are clearly seen in the Na I D lines of HD 190073 and HD 150193 in form of the PCyg-structure.

4.3 Balmer jump

Fig. 7 illustrates the normalized spectra of the targets in the region of the Balmer jump in comparison with spectra of non-accreting stars of similar spectral types. Castelli-

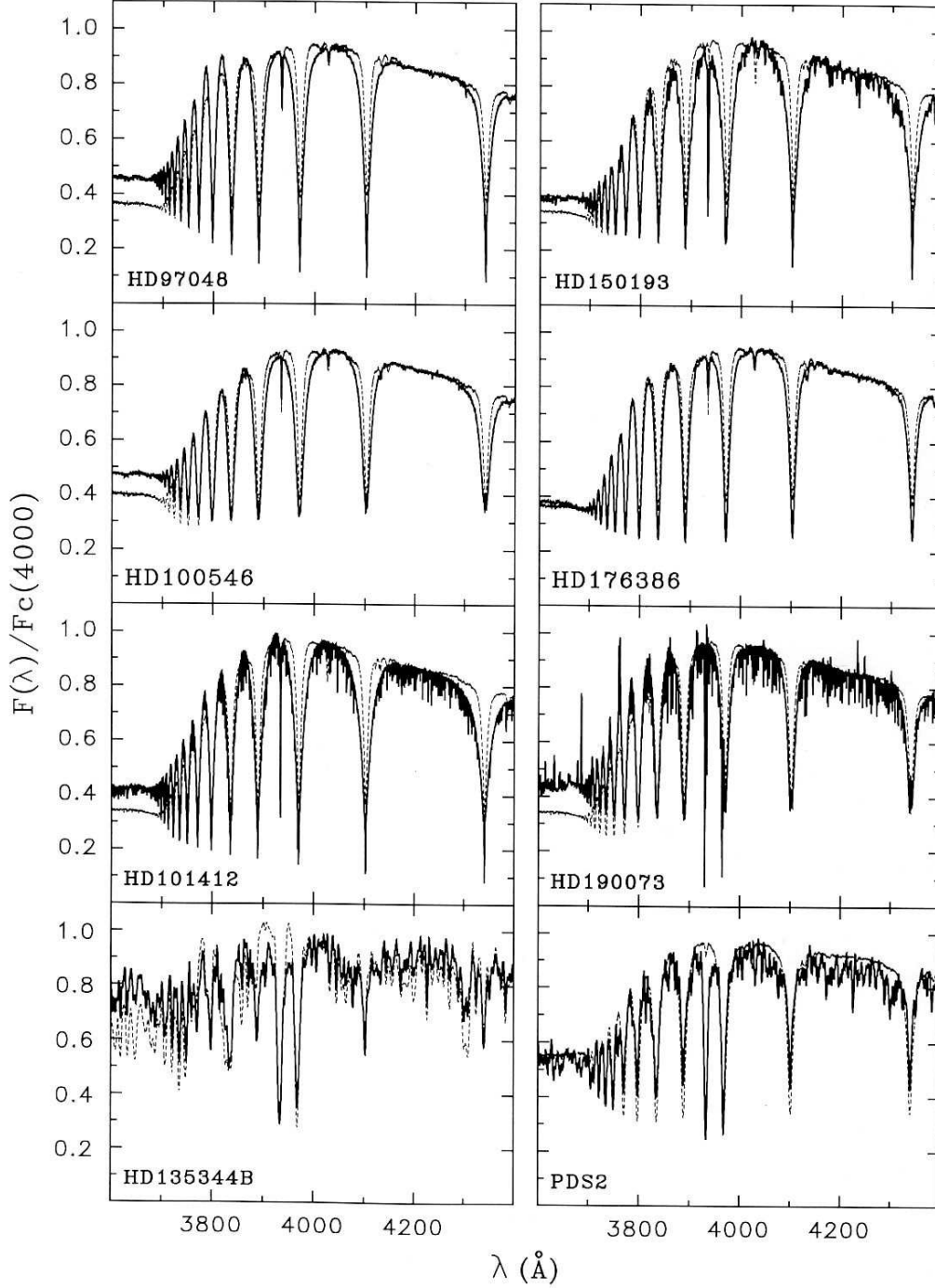


Fig. 7 Normalized spectra of our targets in the region near 3600–4400 Å. The normalization was made to the flux $F(\lambda)$ at the level of the model continuum at $\lambda = 4000$ Å. Spectra of standards of similar spectral type are given for comparison (dashed lines).

Kurucz LTE (Castelli & Kurucz 2008) models were applied for normalization of the observed spectra of non-accreting stars to flux F_λ at 4000 Å at the continuum level. The r -dependencies (see Sect. 3 and Fig. 3) were used to construct the normalized spectra of the targets.

The EWs of all studied lines, the H α 10% width and ΔD_B are listed in Table 5 together with the observing

dates and magnetic/rotation phases calculated according to the ephemerides presented in Hubrig et al. (2011a, 2011b). Mean accuracies of the measurements are presented in Table 6. The errors of the individual estimates of the equivalent widths were computed using a program that takes into account the width and the maximum intensity of an emission line as well as the S/N ratio of the spectrum near the mea-

Table 5 Observing dates, magnetic/rotation phases calculated according to the ephemerides presented in Hubrig et al. (2011a, 2011b), and measurement results of EWs, $W(\text{H}\alpha 10\%)$, and ΔD_B for HAes in our sample.

Object	MJD	Magn. phase	Br γ	Pa β	Pa γ	EW [Å]		H α	Na I D	He I 5876	H β	$W(\text{H}\alpha 10\%)$ [km/s]	ΔD_B
HD 97048	55352.000	0.43	10.30	21.90	9.12	—	—	30.8	—	0.0525	1.58	604	0.25
HD 100546	55352.022		16.05	26.41	9.72	—	—	30.7	0.035	0.162	2.55	540	0.18
HD 101412	55351.992	0.71	5.79	7.77	3.63	—	—	13.6	0.340	0.145	1.69	560	0.225
HD 135344B	55329.362		2.27	3.88	1.47	—	—	10.3	—	0.43	1.57	496	0.15
	55352.034		3.21	4.10	1.72	—	—	14.5	—	0.32	2.16	501	0.15
	55357.251		2.65	3.21	1.39	—	—	11.1	—	0.26	2.00	501	0.15
HD 150193	55329.371	0.59	8.83	7.66	4.93	0.87	1.61	11.9	0.253	0.530	1.15	517	0.19
	55352.047	0.81	10.19	9.80	6.06	1.06	2.13	13.6	0.479	0.479	1.50	561	0.19
HD 176386	55329.387	0.09	0.392	0.188	—	—	—	0.167	—	—	—	—	—
	55463.171	0.88	0.184	0.144	—	—	—	0.159	—	—	—	—	—
	55465.138	0.06	0.270	0.203	—	—	—	0.175	—	—	—	—	—
	55466.166	0.21	0.231	0.153	—	—	—	0.161	—	—	—	—	—
HD 190073	55329.397		9.97	15.8	8.04	5.50	6.58	23.9	1.94	0.213	2.64	—	0.19
	55410.250		10.67	18.8	9.45	5.91	7.29	26.8	2.25	0.337	3.54	—	0.27
	55446.078		10.97	19.1	9.74	5.48	6.87	25.2	2.14	0.471	3.58	—	0.27
	55463.182		8.91	18.1	8.36	4.65	5.93	20.5	1.83	0.364	2.37	—	0.185
	55465.159		8.65	17.2	8.67	4.73	5.92	20.5	1.82	0.257	2.56	—	0.19
	55468.141		8.40	16.4	7.82	4.53	5.56	20.5	1.79	0.317	2.18	—	0.19
PDS 2	55375.418		1.60	0.627	0.358	—	—	3.16	—	0.0286	0.34	380	—
	55408.317		—	—	—	—	—	5.69	—	0.0745	0.68	348	—
	55409.410		—	—	—	—	—	5.52	—	0.0585	0.54	380	—
	55410.343		—	—	—	—	—	4.50	—	0.0464	0.32	396	—
	55411.394		2.85	2.05	0.829	—	—	5.90	—	0.1068	0.74	365	—
	55446.307		2.33	1.00	0.450	—	—	3.30	—	0.0621	0.28	424	—
	55463.210		2.77	1.30	0.627	—	—	5.25	—	0.0734	0.55	425	—
	55464.208		1.79	0.95	0.460	—	—	6.10	—	0.0335	0.33	409	—

Table 6 Mean errors of measurements presented in Table 5.

Object	$\pm\sigma(\text{EW})$ [Å]					$W(\text{H}\alpha 10\%)$					ΔD_B
	Br γ	Pa β	Pa γ	Ca II 8662	Ca II 8542	H α	Na I D	He I 5876	H β	[km/s]	[mag]
HD 97048	0.25	0.40	0.25	—	—	0.45	—	0.015	0.10	20	0.03
HD 100546	0.30	0.40	0.25	—	—	0.45	0.015	0.020	0.15	20	0.03
HD 101412	0.20	0.25	0.20	—	—	0.30	0.05	0.030	0.10	20	0.03
HD 135344B	0.15	0.15	0.10	—	—	0.25	—	0.045	0.10	20	0.03
HD 150193	0.25	0.25	0.20	0.07	0.10	0.25	0.04	0.060	0.10	20	0.03
HD 176386	0.08	0.05	—	—	—	0.05	—	—	—	—	—
HD 190073	0.25	0.30	0.25	0.15	0.20	0.40	0.10	0.04	0.15	—	0.03
PDS 2	0.10	0.10	0.06	—	—	0.20	—	0.02	0.06	20	—

sured line. Further, the program considers the contribution of the photospheric background and the telluric line subtraction. Since we used for the determination of ΔD_B a method similar to that used by Donehew & Brittain (2011), our error estimates are of the same order as presented by these authors, about 0.03 mag. The errors for the individual measurements differ from the mean values presented in Table 6 by not more than 20%.

5 Accretion rates

5.1 Testing existing empirical calibrations

We computed the \dot{M}_{acc} values for HAes in our sample using the measured quantities from Table 4 for indicators specified at the beginning of Sect. 4.

HD 176386 was excluded from our analysis for the reason discussed in Sect. 4.1. The formal calculation of \dot{M}_{acc} of this object leads to $\log \dot{M}_{\text{acc}} = -8.70$ for Br γ , -9.03

for $\text{Br}\beta$, and -9.63 for $\text{H}\alpha$. Other indicators are absent in all observed spectra of the star or too weak to be measured precisely.

The indicator ΔD_B was used only for six objects with $\dot{M}_{\text{acc}} > 10^{-8} M_{\odot}/\text{yr}$. As was concluded in Donehew & Brittain (2011), this diagnostics is inefficient for $\Delta D_B < 0.1^m$. The width $\Delta V(\text{H}\alpha 10\%)$ cannot be measured correctly for HD 190073 because a strong P Cyg-type structure overlaps the blue wing of the emission $\text{H}\alpha$ profile. Taking into account that such features are not common to all HAes, there is a doubt if it is reasonable to use them at all. Still, it is of interest to compare the \dot{M}_{acc} estimations derived from these diagnostics with values obtained from other indicators.

5.1.1 Criterion of applicability

Our aim was to choose diagnostics that lead to results consistent with each other, where the basic indicator ΔD_B is the only tracer connected with \dot{M}_{acc} directly on the basis of model calculations. We introduce the criterion of applicability of a diagnostic “X” for measuring the \dot{M}_{acc} of HAes as follows: the indicator is applicable if the mean value of $\langle \log \dot{M}_{\text{acc}}(\Delta D_B) - \log \dot{M}_{\text{acc}}(X) \rangle$ (further in the text as “ $\Delta D_B - X$ ”) is consistent with zero within the $1 \sigma_m$ errors, calculated for our sample. Here $\sigma_m = \sigma / \sqrt{n - 1}$ is the standard error of the mean value and n is the number of objects.

As a result, we identified a number of diagnostics satisfying this criterion (see Table 7). A small disagreement is present in the $\text{Pa}\beta$ (Dahm 2008) indicator: $+0.30 \pm 0.09$ dex, and in the $\text{Ca II } \lambda 8542(\text{L})$ (Dahm 2008) indicator. In any case, the mean spread of all these differences type “ $\Delta D_B - X$ ” is of the order of ± 0.10 – 0.15 dex. It is remarkable that if the lines Na I D and $\text{IR Ca II } \lambda 8542$ are clearly visible in the spectrum of an object, the \dot{M}_{acc} estimates derived from these indicators are in a satisfactory agreement with values obtained from other spectral diagnostics.

The three remaining indicators of \dot{M}_{acc} that make use of F-type calibrations ($\text{Ca II } \lambda 8542$, $\text{Ca II } \lambda 8662$, and $\text{He I } \lambda 5876$) were additionally examined because the “ $\Delta D_B - X$ ” values of two Ca II (F) indicators demonstrate differences at larger amplitudes than all other tracers presented in Table 7: $(+0.44 \pm 0.32 \text{ dex and } -0.28 \pm 0.35 \text{ dex for Ca II } \lambda 8542 \text{ (F) and Ca II } \lambda 8662 \text{ (F), respectively})$. Further, the $\text{He I } \lambda 5876$ tracer shows a notable systematic shift of “ $\Delta D_B - X$ ” = $+0.69 \pm 0.19$ dex.

5.1.2 Testing F-calibrations

The analysis of \dot{M}_{acc} estimates that were obtained using these diagnostics demonstrate considerable systematic inconsistencies between each other as well as between F- and L-type calibrations for the same lines. These discrepancies are illustrated in Fig. 8.

The estimates derived from $\text{Ca II } \lambda 8542(\text{F})$ are systematically 0.75 ± 0.03 dex higher than those from Ca II

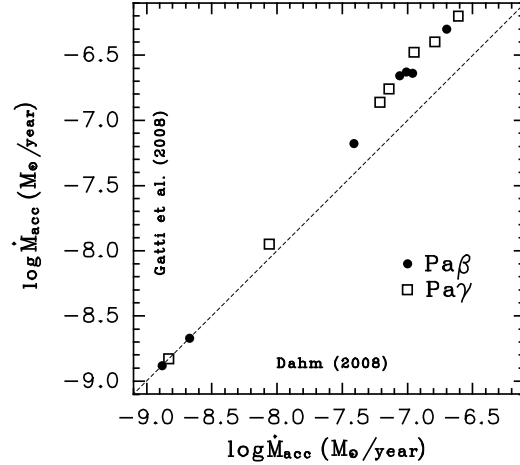


Fig. 9 Comparison of the results of the $\log \dot{M}_{\text{acc}}$ [dex] determination for our targets obtained from the different $\text{Pa}\beta$ and $\text{Pa}\gamma$ calibrations defined in Dahm (2008) and Fang et al. (2009). The dashed line indicates the equality of measured values.

$\lambda 8662(\text{F})$ (top left panel). These two lines originate in the same circumstellar region, and we conclude that conditions in this region in HAes are different from those in TTS for which these two F-calibrations have been introduced.

The mean difference between values obtained from $\lambda 8542(\text{F})$ and $\lambda 8542(\text{L})$ is $+0.90$ dex for HD 190073 and $+0.40$ dex for HD 150193 (top right panel). A similar picture is observed if we compare the \dot{M}_{acc} derived with $\text{He I } \lambda 5876(\text{F})$ and $\text{He I } \lambda 5876(\text{L})$ calibrations (bottom panel). The values obtained with the F-type calibrations are systematically higher with the spread lying between 0.15 and 0.70 dex for different objects. Each star has its own offset which is the same at all observed epochs pointing at some systematic factor. Based upon the results of this test, we assume that the L-type calibrations are best suitable for the HAes in our sample. We suggest that the observed systematic differences between the values derived with the F- and L-type calibrations are likely to be caused by an insufficient accuracy of the c and d coefficients in the F-type calibrations applied to HAes, as well as by uncertainties in M_* or R_* of the targets, used for the calculation of L_{acc} .

5.1.3 Other factors leading to systematic effects

The uncertainties in stellar parameters (especially in the stellar radius R_*) can be a source of considerable systematic errors in the \dot{M}_{acc} determination. As an example, we computed the mass accretion rate of HD 190073 separately with two different values of its stellar radius: $R_*/R_{\odot} = 3.6$ (Catala et al. 2007) and the more recent estimate $R_*/R_{\odot} = 2.1$ (Montesinos et al. 2009). In the first case, we have obtained a mean value of the accretion rate -6.23 , with a spread at the level of standard deviation of ± 0.17 dex using eight spectral indicators derived from luminosities of the emission lines (L-type). This value strongly deviates from

Table 7 List of diagnostics satisfying our criterion of applicability (besides of ΔD_B). The error of the mean value σ_m indicates the accuracy of determination.

Diagnostic “X”	Reference	Mean value of “ $\Delta D_B - X$ ”	Number of objects
		[dex]	<i>n</i>
Br γ (L)	Donehew & Brittain (2011)	$+0.19 \pm 0.15$	6
Pa β (L)	Dahm (2008)	$+0.30 \pm 0.09$	6
Pa γ (L)	Dahm (2008)	$+0.11 \pm 0.15$	6
H α (L)	Dahm (2008)	-0.02 ± 0.12	6
H β (L)	Dahm (2008)	-0.13 ± 0.09	6
He I $\lambda 5876$ (L)	Fang et al. (2009)	$+0.17 \pm 0.17$	6
Na I D(L)	Herczeg & Hillenbrand (2008)	$+0.10 \pm 0.16$	3
Ca II $\lambda 8542$ (L)	Dahm (2008)	-0.22 ± 0.07	2
H α 10%	White & Basri (2003)	$+0.08 \pm 0.10$	5

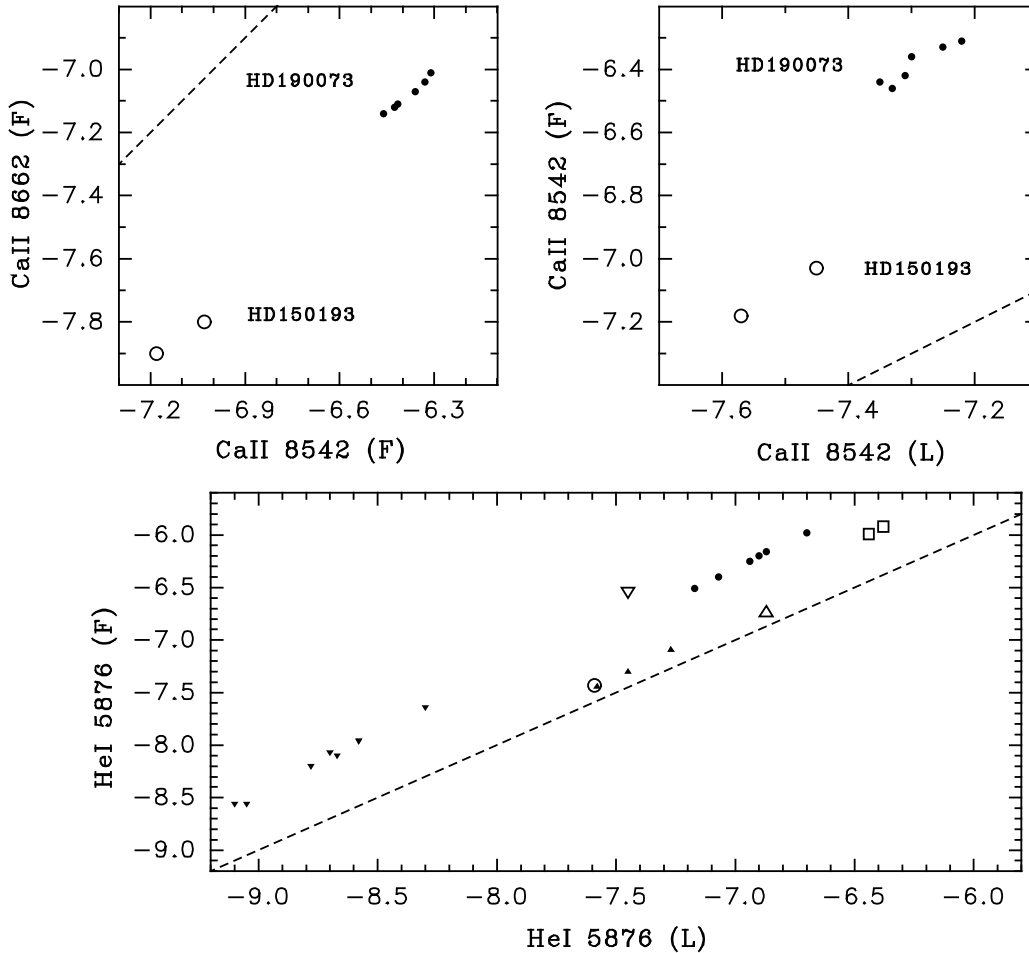


Fig. 8 Illustration of systematic discrepancies between the results of the $\log \dot{M}_{\text{acc}}$ [dex] determination obtained from comparing three pairs of diagnostics: Ca II $\lambda 8542$ (F) vs Ca II $\lambda 8662$ (F) (left top panel); Ca II $\lambda 8542$ (L) vs Ca II $\lambda 8542$ (F) (right top panel); and He I $\lambda 5876$ (L) vs He I $\lambda 5876$ (F) (bottom panel). The dashed lines indicate the position of equality of abscissa and ordinate. Results for different objects are marked by different symbols. In the upper panels the filled circles mark the six measurements for HD 190073, while open circles refer to measurements obtained for HD 150193. Ca line diagnostics can be used only for these two stars. In the bottom panel HD 97048 is marked by the open circle, HD 100546 by the open triangle pointing downwards, HD 101412 by the open triangle pointing upwards, HD 135344B by filled triangles pointing upwards, HD 150193 by open squares, HD 190073 by filled circles, and PDS2 by filled triangles pointing downwards.

the -7.14 obtained from ΔD_B which, according to Fig. 1, is independent of M_* and R_* of a star. Using $R_* = 2.1 R_\odot$ leads to the mean value -7.15 ± 0.17 , that is in good agreement with the estimation from ΔD_B .

Applying different empiric relations between $\text{Pa}\beta$ and $\text{Pa}\gamma$ luminosity, respectively, and the mass accretion rates that have been derived for the TTS by various authors to our sample, we find considerable and systematic discrepancies. This is demonstrated in Fig. 9 where we show the \dot{M}_{acc} values for the targets that result from the calibrations by Gatti et al. (2008) versus those from Dahm (2008). As can be seen in Fig. 9, the difference between the two calibrations is practically absent for small $\log \dot{M}_{\text{acc}}$ (less than -8.0) and becomes up to 0.40 dex for $\log \dot{M}_{\text{acc}} > -7$. We have to mention that Gatti et al. (2008) have calibrated their relation over the $\log \dot{M}_{\text{acc}}$ range from -9.6 to -8.2 (M_* range 0.1 – $1.0 M_\odot$) and Dahm (2008) from -8.7 to -7.2 (M_* range 0.5 – $2.0 M_\odot$), that is more similar to values \dot{M}_{acc} and M_* for our targets. Therefore, we used in our study the diagnostics $\text{Pa}\beta(\text{L})$ and $\text{Pa}\gamma(\text{L})$ introduced by Dahm (2008).

5.2 The deduced accretion rates for the targets in our sample

Fig. 10 illustrates the mass accretion rates obtained for seven program stars (except HD 176386) that have been derived using the indicators that passed successfully our applicability test (see Sect. 5.1.1). Because the F-type diagnostics lead to systematic differences in the \dot{M}_{acc} estimates in comparison with the values obtained with the other indicators (see Sect. 5.1.2 and Fig. 8), we did not include the values of \dot{M}_{acc} derived from F-type indicators in the calculations of the mean values and the uncertainties of the mass accretion rates. As a result, only L-type indicators were used (except $H\alpha 10\%$ and ΔD_B) and, further in the text, we dropped the abbreviation (L) in the names of the indicators.

The mean values of \dot{M}_{acc} over the observed epochs and over several diagnostics as well as their standard deviations are presented in Table 8, where estimates from Garcia Lopez et al. (2006) and Mendigutia et al. (2011a) are also given for comparison. One can see that, in spite of the fact that the observations of Garcia Lopez et al. (2006) were carried out in 2004, the discrepancies are within the limits of the standard deviations obtained in both works. On the other hand, the results obtained in Mendigutia et al. (2011a) demonstrate significant differences with our estimates. The difference is $+0.94$ dex for HD 150193 and $+2.15$ dex for HD 190073. Using data on A_V , $L(H\alpha)$, and $L(Br\gamma)$ presented in Mendigutia et al. (2011a) and from our paper, we estimated contributions of various factors forming the total discrepancy. These contributions are: $+0.2$ – 0.3 dex follow from differences in fluxes measured on different dates, $+0.4$ – 0.5 dex result from distinctions in \dot{M}_{acc} calibrations (for both HD 150193 and HD 190073). The contributions from differences in adopted stellar parameters M_* and R_* are $+0.2$ dex and $+1.5$ dex for HD 150193 and HD 190073,

respectively. Such a significant discrepancy for HD 190073 is mainly related to the very large value of the stellar radius, $R_* = 8 R_\odot$, used in Mendigutia et al. (2011a). This radius is by a factor of four larger than the value adopted in our work (Table 2).

We note that the existence of a HAeBe with T_{eff} less than $10\,000$ K, $M_* = 5.1 M_\odot$, and $R_* = 8 R_\odot$ (Mendigutia et al. 2011a) is not consistent with the PMS evolution model by Palla & Stahler (1993). According to their model, a PMS object with the initial $M_* = 5 M_\odot$ starts to become visible at the birthline with T_{eff} of about $12\,000$ K, and later, closer to the end of the PMS stage near the main sequence, its effective temperature will become about $16\,000$ K. With the age of about 10^6 years given for HD 190073 in Hubrig et al. (2009) and Mendigutia et al. (2011a), the star has to be located in the H-R diagram already near the main sequence, and with $M_* = 2$ – $3 M_\odot$ (Table 2) its stellar radius R_* cannot be as large as $8 R_\odot$.

As was discussed in Sect. 2.2, the \dot{M}_{acc} calibrations derived in Mendigutia et al. (2011a) lead to very large values of the mass accretion rates for a considerable part of their targets, which are not in agreement with the masses of accretion disks (0.01 – $0.1 M_\odot$) and the length in time of the PMS stage for HAes (10^5 – 10^6 years). They demonstrate also significant differences with the results of Donehew & Brittain (2011) and Garcia Lopez et al. (2006).

Our \dot{M}_{acc} determination is based on:

- consistence of values derived from several independent calibrations,
- agreement of our estimates with those obtained in Garcia Lopez et al. (2006), and
- accordance of our results with the predictions of the PMS evolution model by Palla & Stahler (1993).

Clearly, for HAEs with accretion disk masses of the order of 0.01 – $0.1 M_\odot$ and a length of the PMS stage of HAEs of 10^5 – 10^6 years, the expected mean accretion rates during the PMS stage are of the order of 10^{-6} – $10^{-8} M_\odot/\text{yr}$. These expected rates are similar to the values obtained in our work.

Comparing the accuracy of our estimates with the results obtained by other authors, we can see that the differences are not significant (see Table 9).

6 Variability of the mass accretion rates

Four out of seven of our targets were observed on more than one occasion (from two to eight). As was discussed in the previous sections, all emission lines chosen as indicators of \dot{M}_{acc} are formed not only in the magnetosphere, but also in the disk and in the wind, and their contribution to the entire emission is different for each line. Investigating a temporal behaviour of \dot{M}_{acc} using different spectral diagnostics, we have to be certain that a variability revealed from these indicators relates to a change of \dot{M}_{acc} and not to variations of physical and kinematical conditions in the disk and

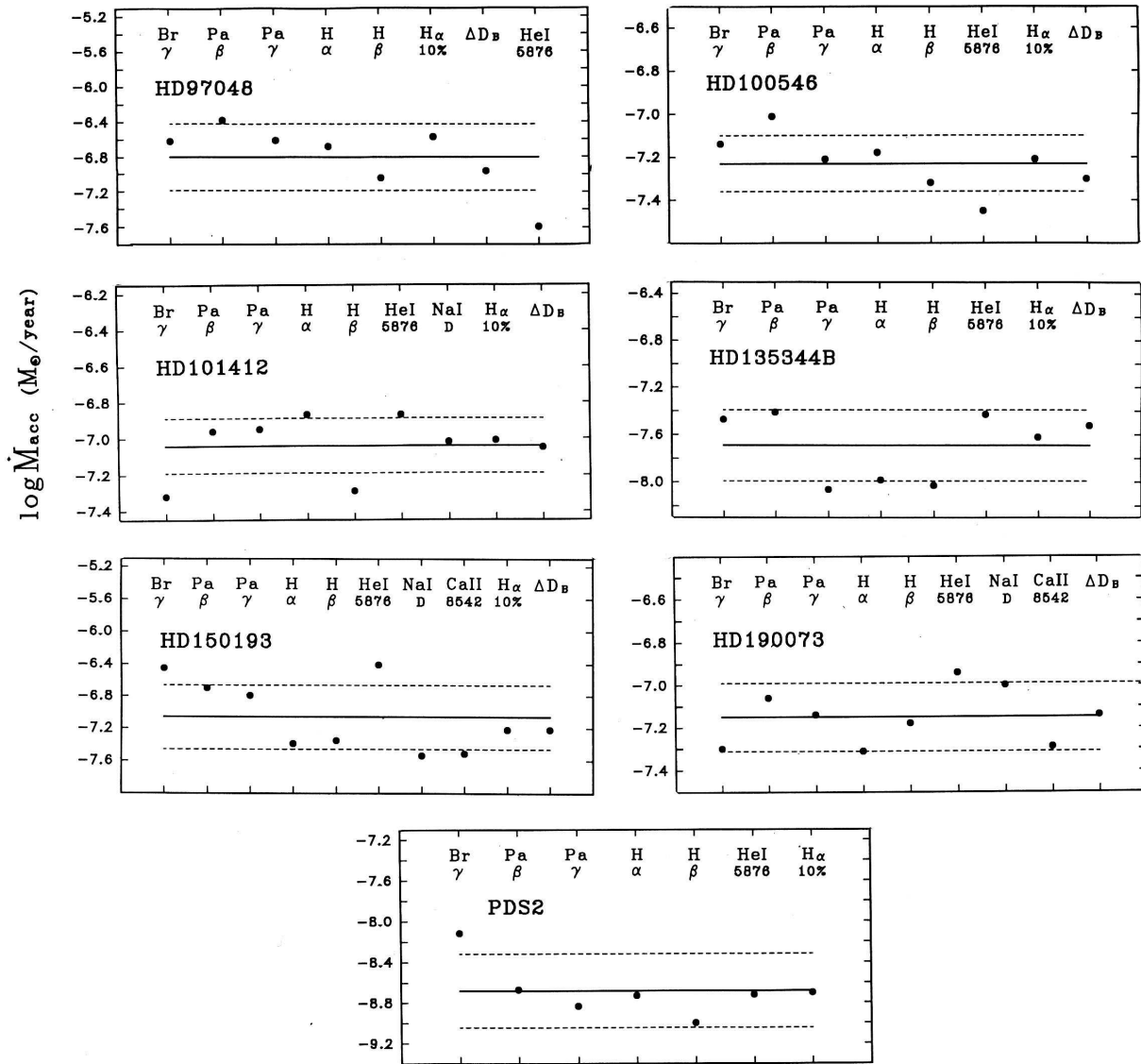


Fig. 10 Mass accretion rates of the targets determined from different indicators, as labeled. The solid line shows the mean $\log \dot{M}_{\text{acc}}$ value and the dashed lines indicate the region of $\pm 1\sigma$ uncertainty where σ is the standard deviation.

Table 8 Mean mass accretion rates. The error is given as the standard deviation σ . Literature data on accretion rates are taken from Garcia Lopez et al. (2006) and Mendigutia et al. (2011a).

Object	Number of indicators	Number of observations	$\log \dot{M}_{\text{acc}}$ [M_{\odot}/yr]	$\log \dot{M}_{\text{acc}}$ [M_{\odot}/yr]	$\log \dot{M}_{\text{acc}}$ [M_{\odot}/yr]
				Garcia Lopez et al. (2006)	Mendigutia et al. (2011a)
HD 97048	8	1	-6.80 ± 0.38	-7.17	
HD 100546	8	1	-7.23 ± 0.13		
HD 101412	9	1	-7.04 ± 0.15		
HD 135344B	8	3	-7.69 ± 0.30	-8.27	
HD 150193	10	2	-7.06 ± 0.20	-7.29	-6.12
HD 190073	9	6	-7.15 ± 0.16		-5.00
PDS 2	7	8	-8.68 ± 0.36		

Table 9 Mass accretion rate determinations using several diagnostics presented in this work and the results published in the literature.

Paper	Range of $\log \dot{M}_{\text{acc}}$ [M_{\odot}/yr]	Range of individual deviations [dex]	Mean standard deviation σ [dex]	Error of the mean value σ_m [dex]
This paper	$-8.68 \div -6.69$	0.13 – 0.36	0.25	0.11
Dahm (2008)	$-8.72 \div -7.20$	0.1 – 1.4	0.30	0.12
Rigliaco et al. (2011)	-9.86	0.4 – 1.4	0.45	0.14

the wind. For example, the emission in such lines as H α , H β , and DNa I originates predominantly in the wind, while that in the He I line and near the Balmer jump in the high-temperature region close to the stellar surface (Pogodin et al. 2012). If the variations take place particularly in the outer circumstellar envelope, they are reflected differently in each of these lines. As a result, the amplitudes and even the character of the measured \dot{M}_{acc} variability derived from different spectral calibrations can be different too. In such a situation, the revealed changes of \dot{M}_{acc} must be considered as an artifact.

6.1 Temporal behaviour of individual accretion diagnostics

Fig. 11 illustrates variations of \dot{M}_{acc} of the two targets HD 190073 and PDS 2 with the largest number of observations determined from all indicators. Since the amplitudes of the variability are smaller than the discrepancies between the values obtained from different diagnostics, we analyzed not the values themselves but the residuals relative to the mean value for each indicator. As one can see in Fig. 11, both objects demonstrate variability which: (a) correlates in a majority of the indicators, and (b) shows amplitudes of the variations that are very similar for different diagnostics. It could be intrinsic \dot{M}_{acc} variability but also some geometric effect that affects in the same way our view of all the different emitting regions.

However, one indicator exists for both objects showing a distinct temporal behaviour of \dot{M}_{acc} : it is He I $\lambda 5876$ for HD 190073 and H α 10% for PDS 2. The character of the variability of the \dot{M}_{acc} value from the He I line in the spectrum of HD 190073 is similar in comparison with other indicators, but shows a much larger amplitude. In the case of PDS 2, the estimations derived from the H α 10% width strongly differ from all others. A possible cause for this can be related to the existence of small-amplitude variations taking place in the circumstellar gas outside the magnetosphere (the outer disk and the wind) which may influence the full width of the profile but might be insufficient to have a significant effect on the EW of H α . This could explain a rather small distorting influence of the non-magnetospheric variability onto the \dot{M}_{acc} derived from the H α (L) diagnostic and a rather significant – onto that obtained with the H α 10% indicator.

The other two stars with more than one available spectrum, HD 150193 and HD 135344B, demonstrate the temporal behaviour of \dot{M}_{acc} derived from all calibrations that is similar to the case of HD 190073. The only exception is the He I $\lambda 5876$ diagnostic. Variability of \dot{M}_{acc} values derived from this indicator is quite different from that obtained from all other indicators. Presently, no strict model for the formation of the He I $\lambda 5876$ line in the high-temperature circumstellar gas around HAeBes exists. We can only assume that a multi-component variability is likely taking place that is connected with a change of geometric configuration, optical thickness and emissivity of the gaseous flows accreted onto the star inside the magnetosphere. But this has a rather small amplitude and the mean value derived from He I differs not so strongly from all the others estimates (see Fig. 10).

6.2 Global accretion variations

As a measure for the overall accretion variability, Fig. 12 illustrates the temporal behaviour of the mean values of \dot{M}_{acc} for the four targets derived from several diagnostics. The error of the mean value $\sigma_m = \sigma / \sqrt{n - 1}$ (where σ is the standard deviation and n is the number of the used diagnostics) is shown by vertical bars. Indicators showing a temporal behaviour of \dot{M}_{acc} different from all others were excluded from the calculation of the mean values and their errors (these are He I $\lambda 5876$ for HD 190073, HD 135344B, and HD 150193, and H α 10% for PDS 2).

HD 190073 demonstrates variability on the timescale of tens of days with a spread of the values of about 0.1 dex with an accuracy at $1\sigma_m$ level of ± 0.01 dex. Short-term variations (from night to night) are undoubtedly found in PDS 2. The observations of HD 135344B and HD 150193 were carried out only on two to three different nights, separated by several to tens of days. Thus, it is impossible to examine the cause of the variability.

An effective way to analyze the amplitudes and the timescale of accretion variability was suggested by Nguyen et al. (2009), where a change in amplitude versus the time interval between observations was constructed for 40 classical TTS. The authors sampled the timescale range from hours to months and concluded the maximum extent of the \dot{M}_{acc} variability is reached after a few days and amplitudes of variations are as a rule not more than 0.5 dex. This result has been confirmed by other authors. Costigan et al. (2012) bolster it with a sample of 10 accreting TTS observed in

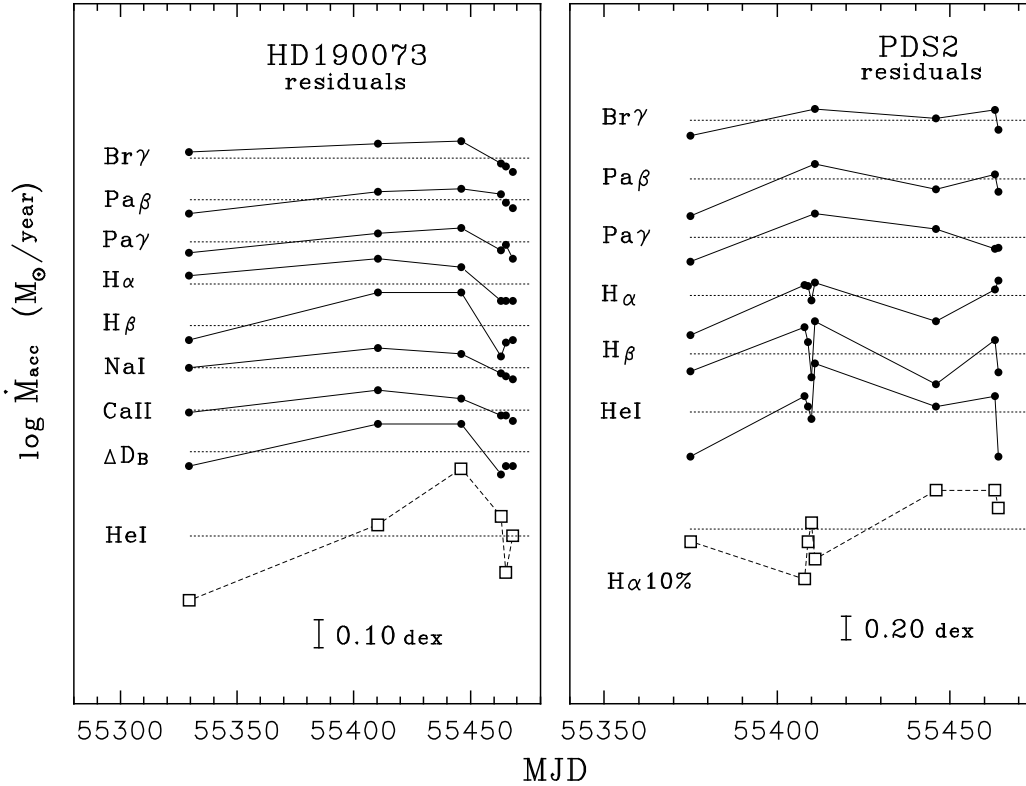


Fig. 11 Temporal behaviour of $\log \dot{M}_{\text{acc}}$ in HD 190073 and PDS 2 obtained from different indicators, constructed relative to the mean value for each indicator. Thin solid lines join neighbour points for each indicator for better illustration. The temporal behaviour of the residuals $\log \dot{M}_{\text{acc}}$ obtained from the indicator He I (for HD 190073, left panel) and from the indicator H α 10% (for PDS 2, right panel) are marked by open symbols and thin dashed lines. Dotted lines indicate positions of zero for each indicator.

the Longterm Accreting Monitoring Project (LAMP) showing that accretion variation amplitudes do not increase when extending the timescales of the monitoring beyond a week.

In Fig. 13 we present our analysis of the \dot{M}_{acc} variability as a function of timescale following Nguyen et al. (2009). Our results are fully in agreement with those obtained previously by other authors. In the case of PDS 2, variations on a timescale of about tens of days with amplitudes of up to 0.4 dex are observed. Besides of that, variability on a timescale near one day is clearly seen with amplitudes of up to 0.3 dex. Such a timescale is comparable with magnetic/rotation periods expected for our targets (Hubrig et al. 2009, 2011a). Therefore variability on such a short timescale is likely to be connected with a modulation of profiles and intensities of the spectral lines by a rotating magnetosphere. Using data from Table 2 (R_* and $v \sin i$), we estimated the rotation period of PDS 2 $P = 2.7 \sin i$ days. This object is likely to be oriented relative to an observer close to “pole-on”, and its inclination angle i is expected to be of order of 15° . Such orientation is confirmed by a single peak emission H α profile (Fig. 4) (see Grinin & Rostopchina 1996).

Due to the insufficient number of observations, it is not possible to analyze the \dot{M}_{acc} variability on different timescales for the other three targets. The only conclu-

sion can be made that a variability has been revealed on timescales from several days to tens of days. In the case of HD 190073 we can derive the rotation period $P = 9.1 \sin i$ days using data from Table 2. In Hubrig et al. (2009) the upper limit of i is given as $i \leq 40^\circ$. A PCyg-type of the H α profile (Fig. 3) evidences that this object has to be of an intermediate orientation relative to an observer (Grinin & Rostopchina 1996). With the expected value of $i \sim 40^\circ$ we estimate $P \sim 6$ days. Since no observations separated by short time intervals have been carried out for this target so far, we cannot examine a presence of rotational modulations of the line profiles in the spectrum of HD 190073.

Another plausible alternative could be that the variability is the result of stochastic variations in the accretion rate through the disk, as one might expect if the magneto-rotational instability is the primary source of viscosity in accretion disks. More spectral data obtained on different timescales (from days to tens of days) are needed to rigorously test the character of the variability of the Herbig Ae/Be stars.

7 Conclusions

We present results of observations of a sample of eight magnetic Herbig Ae stars obtained with the X-shooter spectro-

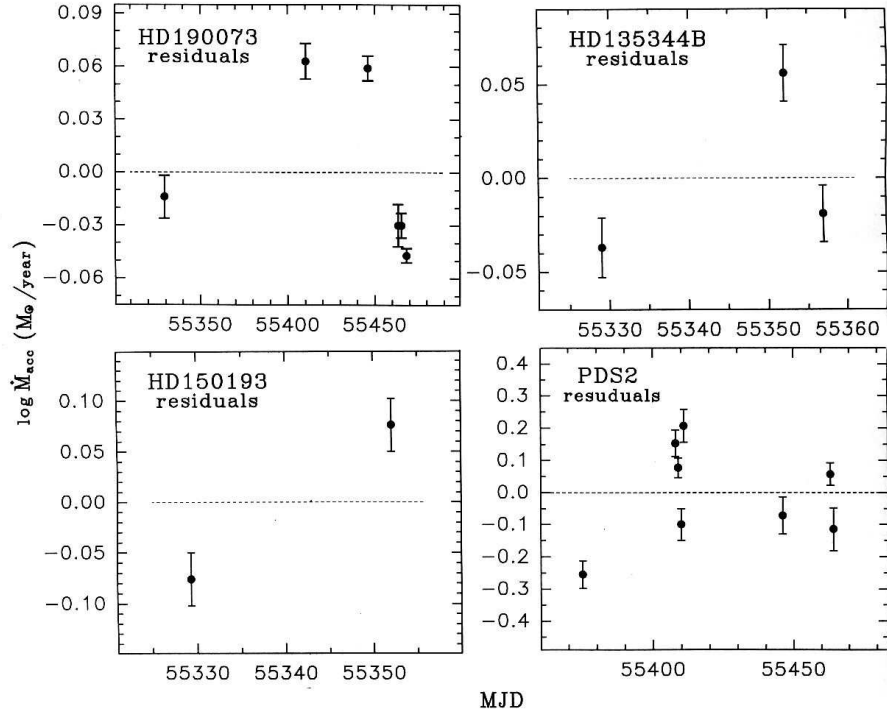


Fig. 12 Temporal behaviour of the mean values of the residual $\log \dot{M}_{\text{acc}}$ of four targets. The errors at $\pm 1\sigma_m$, where σ_m is the error of the mean, are marked by bars. The values are obtained using all indicators for each object (see Fig. 8) except He I (for HD 190073, HD 135344B, and HD 150193) and H α 10% (for PDS 2).

graphs installed on the 8m UT2 at the VLT. This spectrograph covers simultaneously the whole spectral range from the near-UV to the near-IR (300–2500nm), providing medium resolution, high-quality spectra. We examined 13 different spectral accretion diagnostics derived earlier on the basis of TTS and BD observations on their applicability to HAes. This applicability has been confirmed for a number of the indicators. The criterion of the applicability was based on a consistence of the results of \dot{M}_{acc} determination one with another and with the only direct accretion indicator ΔD_B , based on the CS emission near the Balmer jump. We have used the diagnostics satisfying the criterion to compute \dot{M}_{acc} of all targets, which are ranged from 2×10^{-9} to $2 \times 10^{-7} M_{\odot}/\text{yr}$ with standard deviations of 0.25 dex relative to the mean value. The targets in our sample demonstrate a large variety of spectra. One of the eight targets, HD 176386, was excluded from our analysis as an object that has a “non-developed” accretion disk. It was not possible to use all 13 indicators in all objects. The number of the indicators used varies from 7 to 10, depending on the target. An important factor limiting the application of all indicators is the necessity to re-calibrate a number of empiric relations constructed earlier for objects showing small $\dot{M}_{\text{acc}} < 10^{-9} M_{\odot}/\text{yr}$. Their application for HAes with higher ($\dot{M}_{\text{acc}} \sim 10^{-7} M_{\odot}/\text{yr}$) can lead to significant systematic errors. We would like to emphasize that additional future spectral observations of a larger number of HAes are needed to improve all calibrations and to expand

them to the sample of earlier-type PMS objects with higher \dot{M}_{acc} .

An important cause of errors is the uncertainty in determinations of M_* and especially R_* for a number of targets when the indicators are based on luminosity determination. For objects with small accretion rate values ($\log \dot{M}_{\text{acc}} < -8.5$) errors of measurements of EWs and widths of emission profiles become an additional factor for the measurement accuracy.

Our investigation of variability of \dot{M}_{acc} has shown that all four Herbig Ae stars observed on more than one occasion demonstrate a change of \dot{M}_{acc} of about $0.10 \div 0.40$ dex on the timescale of tens of days. One object observed on a short timescale, PDS 2, shows also night-to-night variations with an amplitude of up to 0.30 dex. This variability might be related to the modulation of spectral parameters by a rotating magnetosphere. In the case of even longer-term variability ($\tau \approx$ tens of days) it remains unclear whether this variability is connected with a change in the accretion regime or is a result of rotational modulation. We note that due to the small number of observations of targets with determined magnetic/rotation periods, not much can currently be concluded on the role of magnetic fields in the dynamics of the accretion processes. Future multi-epoch observations of magnetic HAes with X-shooter will be extremely useful to better understand the nature and variability of \dot{M}_{acc} spectral diagnostics to constrain more realistically magnetospheric accretion models for Herbig Ae stars.

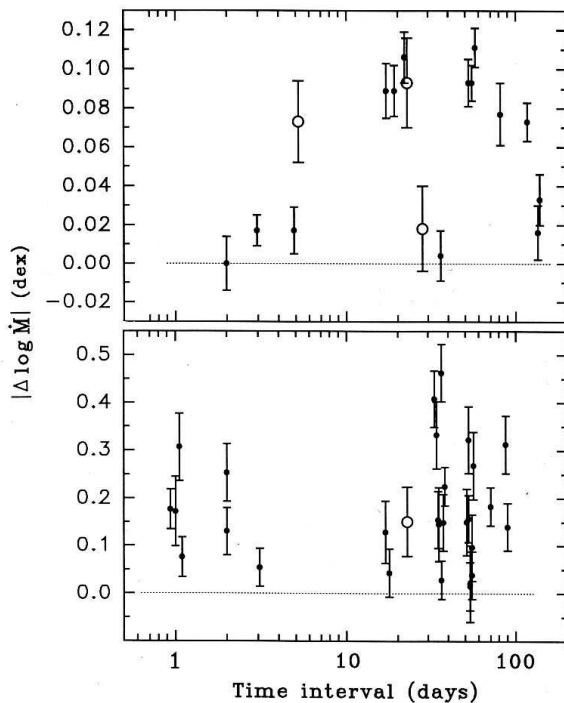


Fig. 13 Amplitude of variations of the mean $\log \dot{M}_{\text{acc}}$ of four targets as a function of time elapsed between the observations. Upper panel: Results for HD 190073 (filled symbols) and HD 135344B (open symbols). Bottom panel: Results for PDS 2 (filled symbols) and HD 150193 (open symbols).

Acknowledgements. MAP and RVY acknowledge Program N21 of the Presidium RAS and Sci. Scale N1625.2012.2.

References

- Ardila, D. R., Basri, G., Walter, F. M., et al.: 2002, *ApJ* 567, 1013
 Bibo, E. A., The, P. S., Dawanas, D. N.: 1992, *A&A* 260, 293
 Bohm, T., Catala, C.: 1995, *A&A* 301, 155
 Bouvier, J., Alencar, S. H. P., Harries, T. J., et al.: 2007, in: *Protostar and Planets V*, Univ. Arizona Press, p. 479
 Castelli, F., Kurucz, R. L.: 2008, http://www.stsci.edu/hst/observatory/cdbs/castelli_kurucz_atlas.html
 Catala, C., Alecian, E., Donati, J. F., et al.: 2007, *A&A* 462, 293
 Calvet, N., Gullbring, E.: 1998, *ApJ* 509, 802
 Calvet, N., Muzerolle, J., Briceno, C.: 2004, *AJ* 128, 1294
 Costigan, G., Scholz, A., Stelzer, B., et al.: 2012, *MNRAS submitted*
 Coulson, I. M., Walther, D. M.: 1995, *MNRAS* 274, 977
 D'Alessio, P., Calvet, N., Hartmann, L., et al.: 1999, *ApJ* 527, 893
 D'Alessio, P., Calvet, N., Hartmann, L., et al.: 2001, *ApJ* 553, 321
 Dahm, S. F.: 2008, *AJ* 136, 521
 D'Odorico, S., Dekker, H., Mazzoleni, R., et al.: 2006, in: *Ground-based and Airborne Instrumentation in Astronomy*, SPIE 6269, p. 626933
 Donehew, B., Brittain, S.: 2011, *AJ* 141, 46
 Fang, M., van Boekel, R., Wang, W., et al.: 2009, *A&A* 504, 461
 Finkenzeller, U., Mundt, R.: 1984, *A&ASS* 55, 109
 Garcia Lopez, R., Natta, A., Testi, L., et al.: 2006, *A&A* 459, 837
 Garcia, P. J. V., Ferreira, J., Cabrit, S., et al.: 2001, *A&A* 377, 589
 Gatti, T., Natta, A., Randich, S., et al.: 2008, *A&A* 481, 423
 Grinin, V. P., Rostopchina, A. N.: 1996, *Astron. Reports* 40, 171
 Grady, C. A., Woodgate, B. F., Bowers, C. W., et al.: 2005, *ApJ* 630, 958
 Grady, C. A., Perez, M. R., The, P. S.: 1993, *A&A* 274, 847
 Grady, C. A., Hamaguchi, K., Scheider, G., et al.: 2010, *ApJ* 719, 1565
 Gullbring, E., Muzerolle, J., Calvet, N., et al.: 2000, *ApJ* 544, 927
 Henning, T., Burkert, A., Launhardt, R., et al.: 1998, *A&A* 336, 585
 Herbig, G. H.: 1960, *ApJSS* 4, 337
 Herczeg, G., Hillenbrand, L. A.: 2008, *ApJ* 681, 594
 Hillenbrand, L. A., Strom, S. E., Calvet, N.: 1998, *AJ* 116, 1816
 Hubrig, S., Pogodin, M. A., Yudin, R. V., et al.: 2007, *A&A* 463, 1039
 Hubrig, S., Stelzer, B., Schöller, M., et al.: 2009, *A&A* 502, 283
 Hubrig, S., Schöller, M., Ilyin, I., et al.: 2011a, *A&A* 536, A45
 Hubrig, S., Mikulasek, Z., González, J. F., et al.: 2011b, *A&A* 525, L4
 Mendigutia, I., Calvet, N., Montesinos, B., et al.: 2011a, *A&A* 535, A99
 Mendigutia, I., Eiroa, C., Montesinos, B., et al.: 2011b, *A&A* 529, A34
 Modigliani, A., Goldoni, P., Royer, F., et al.: 2010, *SPIE* 7737, 56
 Montesinos, B., Eiroa, C., Mora, A., Merin, B.: 2009, *A&A* 495, 903
 Mohanty, S., Jayawardhana, R., Basri, G.: 2005, *ApJ* 626, 498
 Mottram, J. C., Vink, J. S., Oudmaijer, R. D., Patel, M.: 2007, *MNRAS* 377, 1363
 Müller, A., van den Ancker, M. E., Launhardt, R., et al.: 2011, *A&A* 530, 85
 Muzerolle, J., D'Alessio, P., Calvet, N., et al.: 2001, *ApJ* 550, 944
 Muzerolle, J., D'Alessio, P., Calvet, N., et al.: 2004, *ApJ* 617, 406
 Natta, A., Grinin, V. P., Mannings, V., et al.: 2000, in: *Protostars and Planets IV*, 559
 Natta, A., Testi, L., Muzerolle, J., et al.: 2004, *A&A* 424, 603
 Nguyen, D. C., Scholz, A., Marten, H., et al.: 2009, *ApJ* 694, L153
 Oudmaijer, R., van den Ancker, M. E., Baines, D., et al.: 2011, *AN* 332, 238
 Palla, F., Stahler, S. W.: 1993, *ApJ* 418, 414
 Pogodin, M. A.: 1986, *Astrophysics* 24, 279
 Pogodin, M. A.: 1989, *Astrophysics* 31, 506
 Pogodin, M. A., Kozlova, O. V., Ikhsanov, N. R., Yudin, R. V.: 2011, *Astrophysics, submitted*
 Piskunov, N.: 1992, in: *Stellar Magnetism*, Nauka, 92
 Rigliaco, E., Natta, A., Randich, D., et al.: 2011, *A&A* 526, L6
 Tout, C. A., Pringle, J. E.: 1995, *MNRAS* 272, 528
 Tout, C. A., Pringle, J. E.: 1996, *MNRAS* 281, 219
 Wade, G. A., Bagnulo, S., Drouin, D., et al.: 2007, *MNRAS* 376, 1145
 White, R. J., Basri, G.: 2003, *ApJ* 582, 1109